13th International Symposium on Particle Image Velocimetry – ISPIV 2019
Munich, Germany, July 22-24, 2019

Relationship between boundary layer features and shock reflection

R. Baidya*, S. Scharnowski, M. Bross, and C. J. Kähler

Institute for Fluid Mechanics and Aerodynamics, Bundeswehr University Munich,
Werner-Heisenberg-Weg 39, 85577 Neubiberg, Germany

* rio.baidya@unibw.de

Abstract

Large field-of-view (FoV) particle image velocimetry (PIV) experiments are conducted to examine velocity fields in a vicinity of a shock wave boundary layer interaction (SWBLI) at Mach 2. The current FoV covers up to 30 boundary layer thicknesses, comprising of upstream and downstream regions relative to the SWBLI, thereby allowing the turbulent boundary layer features and instantaneous shock locations to be simultaneously captured. The relationship between the boundary layer features and the shock location is directly quantified, with the aim of better understanding the mechanisms responsible for oscillation of the reflected shock. The results show that the reflected shock location is clearly influenced by the instantaneous state of the incoming boundary layer. It is found that a passage of low/high momentum very-large-scale turbulent feature through the SWBLI region causes the reflected shock to move upstream/downstream of the mean location. The results are confirmed by measureing the spanwise characteristics of the shock locations and their influences on the boundary layer features.

1 Introduction

The presence of shock and a turbulent boundary layer in the vicinity of the wall in a supersonic flow results in an interaction region where the two meet. The interaction leads to an extensive modification of the boundary layer immediately downstream of the shock, resulting in the boundary layer to be in a non-equilibrium state where strong gradients exist in the streamwise direction. Such interactions occur on a number of external and internal flow in aerospace applications, and thus needs to be carefully considered when designing components such as airframes and turbomachinery.

In the current work, an interaction between the shock and boundary layer features in a shock reflection configuration is examined (see figure 1). The shock reflection configuration occurs commonly when supersonic flow travels through a duct with opposing side walls, and is typically accompanied by multiple subsequent reflections as the reflected shock from one wall impinges on the opposing wall to form a shock train. The duct flows are ubiquitous in engineering applications, and therefore the ability to accurately predict the resulting shock wave boundary layer interaction (SWBLI) has enormous practical relevance. Despite the high practical relevance, past studies have focused on SWBLI for a compression ramp configuration, with only a few researchers examining the shock reflection configuration, which the current study aims to redress.

One of the notable features of SWBLI is the oscillatory nature of the shock generated in the vicinity of the wall (see figure 4). The shock in the extreme cases can oscillate several boundary layer thicknesses about the mean position (Thomas et al., 1994). This can lead to an elevated surface pressure fluctuation level and instantaneous shock structures that are vastly different from the time-averaged structure (Muck et al., 1985). The resulting unsteadiness, if strong enough, may lead to a catastrophic failure, e.g. structural damage in a supersonic vehicle. While there is a consensus on the relation between the shock oscillation and the expansion and contraction of the separation bubble that forms downstream of the interaction region, the community still remain largely divided on the mechanism explaining the low-frequency unsteadiness, despite multiple investigations on the oscillatory nature of shocks (e.g. Humble et al., 2009; Piponniau et al., 2009). A possible source of discrepancy, at least from the experimental point of view, is that the majority of the past works are based on a single point measurement of velocity/pressure or shadowgraph/schlieren visualization. Hence, the limited nature of these techniques may have led to contrasting conclusions from

M_∞	U_∞ (m s^{-1})	ρ_∞ (kg m^{-3})	$\sqrt{\overline{u^2}}/U_\infty^2$ (%)	p_0 (kPa)	T_0 (K)
2.0	520	0.495	0.7	200	296

Table 1: Experiment freestream parameters.

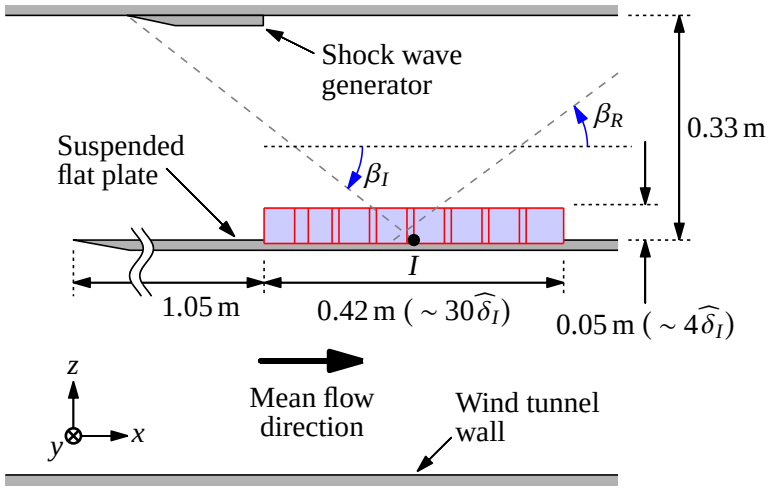

Figure 1: A sketch of the experimental setup. The dashed lines indicate the location of the incident and reflected shock waves, while the blue shaded region shows the combined view from eight cameras (the FoV from each camera is denoted with a red box). β_I and β_R correspond to the angle of the incident and reflected shock relative to the streamwise direction.

different researchers. The current study utilises PIV to capture the shock and the surrounding velocity field simultaneously, thereby allowing the relevant flow physics to be directly quantified.

2 Experimental setup

The experiments are performed in the Trisonic Wind tunnel Munich (TWM) at the Bundeswehr University Munich. This is a blow-down type wind tunnel with a test section measuring 1800 mm × 300 mm × 675 mm along the length, width and height, respectively. An integrated system consisting of an adjustable Laval nozzle and diffuser allows for a stable operation across subsonic, transonic and supersonic regime, with Mach number ranging from 0.3 to 3.0. Moreover, the freestream turbulence intensity varies from 1.9 % to 0.45 % (a decrease in the turbulence level occurs with an increasing Mach number) within the operating range of the wind tunnel (Scharnowski et al., 2019). The facility has two holding tanks that can be pressurized up to 2 MPa above ambient pressure, holding a combined volume of 356 m^3 of dry air. This enables measurement times in the order of 100 seconds for a typical experiment run. The facility is designed to allow the Reynolds number to be independently controlled from the Mach number by changing the stagnation pressure, p_0. The freestream fluid parameters for the current study are outlined in table 1. Here, M_∞, U_∞ and ρ_∞ correspond to the Mach number, mean streamwise velocity and density of the fluid in the freestream region upstream of the shock, while T_0 denote the stagnation temperature.

A flat plate, suspended at the middle of the test section, is used to examine the boundary layer that forms in the vicinity of the plate surface. The incident shock is generated by a shock wave generator in the form of a two-dimensional wedge fixed to the upper wall of the wind tunnel that creates an $11^\circ \pm 1^\circ$ wedge angle with respect to the streamwise direction, as illustrated in figure 1. The passage of supersonic flow around the wedge leads to an oblique shock that impinges on the boundary layer developing along the flat plate at a downstream location, and the location of the incident shock foot is denoted here as I. The current setup differs from past works where the incident shock is generated utilising a two-dimensional obstacle placed in the freestream region (e.g. Dupont et al., 2006), leading to a relatively fixed incident

shock. For the current configuration, the incoming flow to the shock generator is unsteady and contains a wide range of turbulent scales from the boundary layer developing on the roof, therefore resulting in an oscillating incident shock. Oscillating incident shock occur in many practical applications, when multiple shock reflections are generated from two opposing walls, leading to an oscillating reflected shock from one side of the wall to impinge on the opposing wall and acts as an incident shock. Here, U indicate the mean streamwise velocity, while x, y and z denote the streamwise, spanwise and wall-normal directions. Further, tilde operator indicates instantaneous variables, while lower case denotes fluctuations about the mean value. Moreover, x_I denotes the mean streamwise coordinate of the incident shock foot, while $\widehat{\delta_I} = 14.0\,\text{mm}$ (Bross et al., 2019) corresponds to the wall distance at x_I where the mean velocity is equal to 99 % of the incoming freestream velocity, U_∞, for the reference case of zero-pressure gradient compressible boundary layer at a matched Mach number (i.e. without the presence of an incidence or reflected shock).

3 Wall-normal PIV

The flow upstream and downstream of the incident shock foot location, x_I, is captured using planar PIV. In order to facilitate a large field of view (FoV), while still capturing sufficient details of the flow, a multi-camera configuration with eight Imager sCMOS is used, as illustrated in figure 1. This resulted in a combined FoV with dimensions of $0.42\,\text{m} \times 0.05\,\text{m}$ (corresponding to $30\widehat{\delta_I} \times 4\widehat{\delta_I}$) in the streamwise and wall-normal directions, respectively, while still maintaining a scaling of $25\,\mu\text{m}\,\text{pixel}^{-1}$. Furthermore, to allow convergence of conditional mean quantities, about 4700 statistically independent velocity fields are acquired. It should be noted that the illumination for the planar PIV is limited to approximately 1 mm in the spanwise direction, thus the captured instantaneous shock locations are well defined (see figure 4) since only a minuscule variation in the shock location occurs over the illuminated spanwise distance for the PIV images. To enable PIV, the flow is illuminated by a double-pulsed laser sheet generated utilising a Quantel EverGreen laser head, rated at $200\,\text{mJ}\,\text{pulse}^{-1}$. In addition, Di-Ethyl-Hexyl-Sebacat (DEHS) tracer particles with a mean diameter of approximately 1 µm (Kähler et al., 2002) are released into the flow upstream of the settling chamber. The time offset between the double images is set at 1 µs, resulting in a mean particle image shift of 21 pixels in the incoming freestream region. Note that a large pixel shift is important in reducing the relative uncertainty of the PIV measurements, and results from Scharnowski et al. (2019) suggest that a mean shift of 20 pixels or more is desirable. The PIV images are processed using Davis 8.3 software from LaVision GMbH, where multi-pass image deformation and Gaussian window weighting are enabled. The initial and final window sizes corresponding to 128×128 and 16×16, respectively, with a 50 % overlap between the windows are used for the PIV evaluation. To minimise regions of high-intensity pixels in the vicinity of the wall, the aluminium wall surface within the FoV is polished to reduce the light scatter and the cameras positioned to be at a similar height as the wall (Kähler et al., 2012).

Figure 2 shows an exemplary instantaneous streamwise velocity field obtained from the combined FoV for the wall-normal PIV. The large streamwise extent allows the recovery of the modified boundary layer after the shock to be quantified, while capturing $2\widehat{\delta_I}$ region of freestream allows the instantaneous shock locations to be determined (shown in figure 2 as the dashed lines). In addition to the instantaneous shock location, turbulent features within the boundary layer are simultaneously captured, thus providing a unique dataset where interaction between the turbulent features and the shock can be analysed directly.

Figure 3 show the mean streamwise velocity field in the vicinity of the SWBLI region. As noted in the introduction, one of the striking features of SWBLI is the variation in the shock location due to its oscillation, as illustrated in figure 4 where the reflected shock is located upstream and downstream with respect to the mean shock location. Thus, the gradients in the mean field are much more gradual compared to the instantaneous fields as it gets smeared across the region the shock oscillates. Note that the black and grey dashed lines denote the instantaneous and the mean shock locations through out this paper.

To further assess the relation between the state of the incoming boundary layer and the reflected shock location, a subset of the data where the incident shock lies between $\pm 0.25^\circ$ of the mean position (corresponding to 15 % of the total dataset), and therefore remains relatively fixed, is used for the subsequent analysis presented in this section.

3.1 Detection of instantaneous shock locations and boundary layer thicknesses

The shock locations are determined from the local minima at each z location in the instantaneous $\partial\widetilde{U}/\partial x$ fields, as illustrated in figure 5(a). Note that figure 5(a) corresponds to the streamwise gradient of the $\widetilde{U}$ field

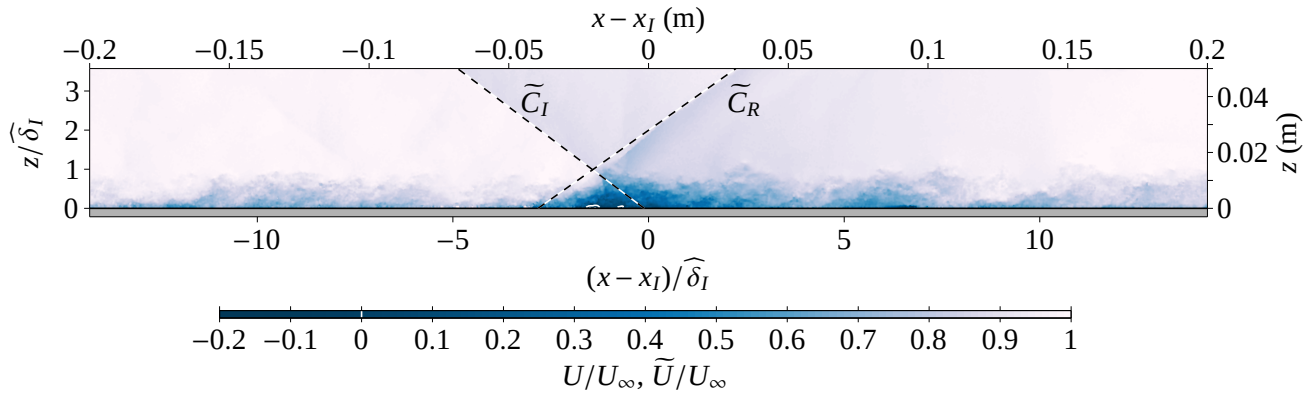

Figure 2: Streamwise–wall-normal view of shock wave boundary layer interaction in a shock reflection configuration. The flow is from left to right, while the colour contours show an instantaneous streamwise velocity field.

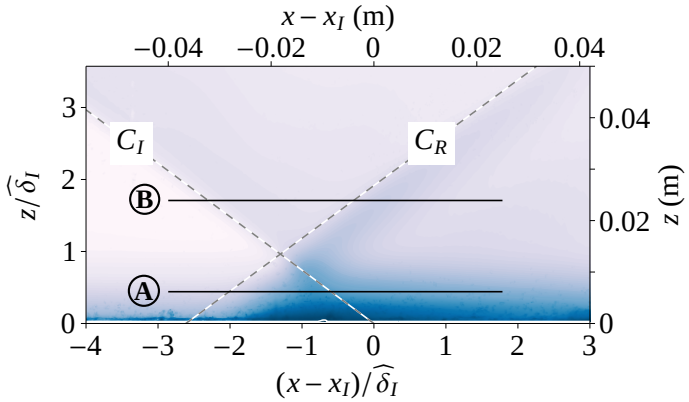

Figure 3: Mean streamwise velocity field, where the colour contours are as in figure 2. The horizontal lines indicate the location of the wall-parallel PIV planes Ⓐ and Ⓑ, at $z/\widehat{\delta}_I \approx 0.4$ and 1.7, respectively.

shown in figure 4(a). From figure 5(a), it is evident that the $\partial\widetilde{U}/\partial x$ assassinated with the the shocks are at a same order of magnitude as near-wall turbulent contributions and therefore hamper the detection of shock locations within the boundary layer. Hence, a linear relation is fitted through the local minima that lie in the freestream region outside the influence of the boundary layer ($z/\widehat{\delta}_I > 1.4$) and extrapolated to the wall.

One parameter that can be used to characterise the state of the boundary layer is the local boundary layer thickness. Locations with low boundary layer thicknesses have fuller velocity profiles compared to locations with high boundary layer thicknesses and therefore are associated with high-momentum events.

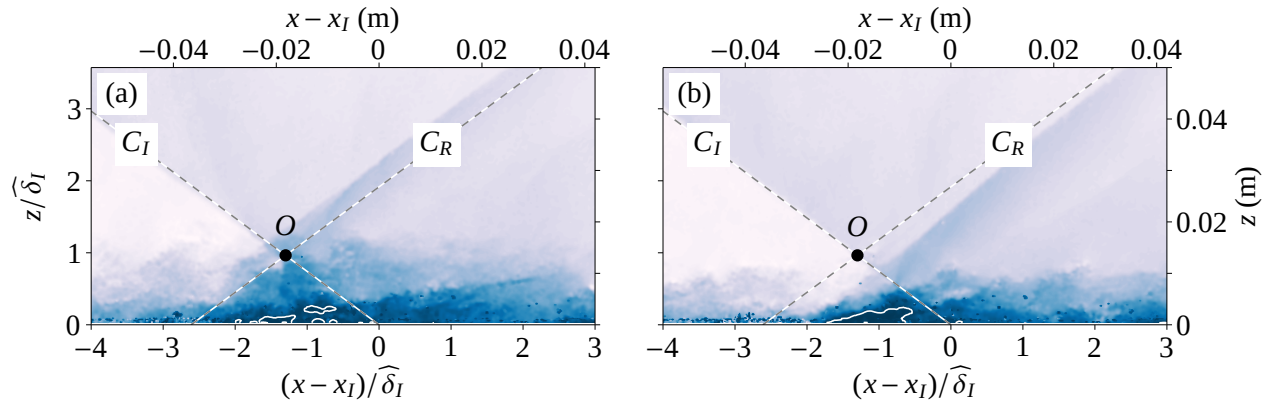

Figure 4: Instantaneous streamwise velocities when the reflected shock is located (a) upstream and (b) downstream of the mean location, C_R, indicated by the dashed line. The colour contours are as in figure 2, while the solid line denotes the $\widetilde{U} = 0$ contour; and the flow is from left to right.

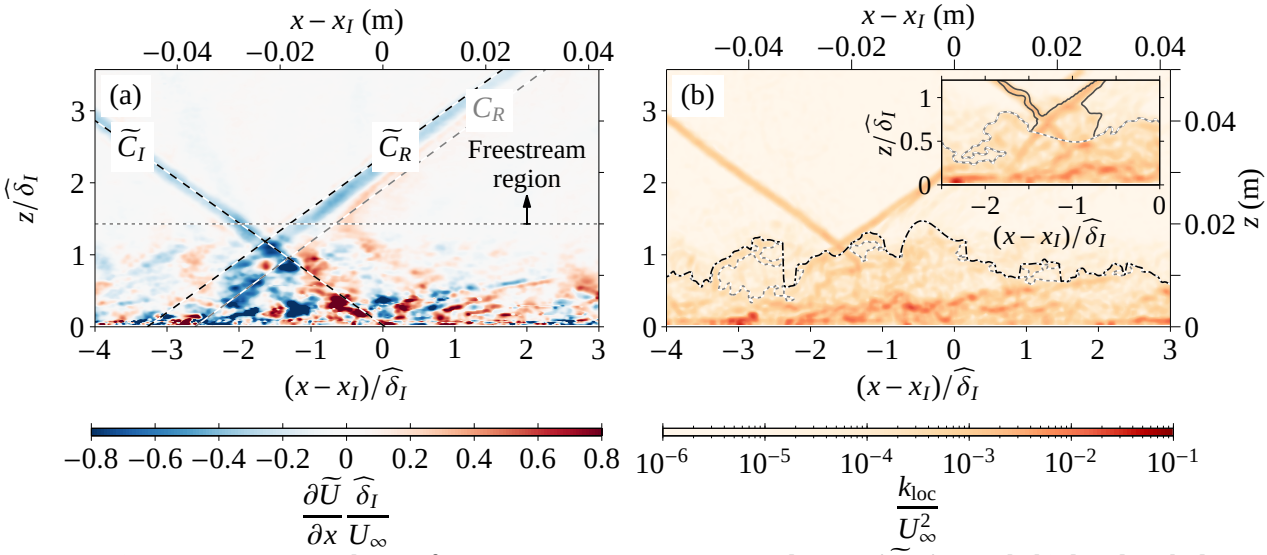

Figure 5: (a) Streamwise gradient of instantaneous streamwise velocity, $\partial\widetilde{U}/\partial x$, and (b) local turbulent kinetic energy, k_{loc}. In (a), the black dashed lines correspond to the instantaneous shock locations, while the mean location of the reflected shock is shown in grey (the instantaneous and mean locations of the incident shock coincide at this instance). In (b), the solid (—), dotted (• • •) and dot-dashed (- • -) lines denote the unadjusted TNTI, adjusted TNTI and TNTI upper envelop locations (following steps 4, 5 and 6), respectively.

The instantaneous boundary between the turbulent flow within the boundary layer and the non-turbulent flow in the freestram region is called the turbulent non-turbulent interface (TNTI), and number of techniques have been purposed to find this interface location in free-shear and wall-bounded flows. Here, we follow a method where a threshold based on a local kinetic energy level is used. The local kinetic energy, k_{loc}, is defined as

$$k_{\mathrm{loc}} = \frac{1}{2N_xN_z}\left[\sum_{i=1}^{N_x}\sum_{k=1}^{N_z}\left(\widetilde{U}_{i,k} - \frac{1}{N_xN_z}\sum_{i=1}^{Nx}\sum_{k=1}^{Nz}\widetilde{U}_{i,k}\right)^2 + \sum_{i=1}^{N_x}\sum_{k=1}^{N_z}\left(\widetilde{W}_{i,k} - \frac{1}{N_xN_z}\sum_{i=1}^{Nx}\sum_{k=1}^{Nz}\widetilde{W}_{i,k}\right)^2\right]. \tag{1}$$

Note that the summations are confined within a rectangular region containing N_x and N_z velocity vectors in the x and z directions, respectively. Furthermore, (1) is a generalised form of the formulation proposed by Reuther and Kähler (2018) and contains an additional contribution from the wall-normal velocity. Hence, k_{loc} is a measure of fluctuation in velocity within the specified rectangular region. That is, k is near zero in freestream region where the flow behaves like a inviscid fluid, while $k \gg 0$ in the turbulent region within the boundary layer. The threshold used here corresponds to $9k_\infty$, where k_∞ corresponds to the median value obtained for the $z/\widehat{\delta}_I > 1.4$ region. This covers ±3 standard deviations ($\sqrt{k_{\mathrm{loc}}} < 3\sqrt{k_\infty}$) and hence corresponds to a 99.7 % certainty level in detecting the freestream region assuming a Gaussian distribution. To extract a TNTI location following steps are performed:

1. k_{loc} is calculated with $N_x = N_z = 9$ following Reuther and Kähler (2018).
2. The mean kinetic energy contribution from the shock is determined by averaging k_{loc} in the region $z/\widehat{\delta}_I > 1.4$. The averaging is performed in the direction parallel to the instantaneous shock.
3. The mean kinetic contribution from the shock is subtracted from k_{loc} at each z location along the instantaneous shock location to mitigate the k_{loc} contribution from the shocks.
4. Thersholding is applied to the modified k_{loc} from step 3 to determine the TNTI.
5. Instances when the detected TNTI has been distorted by the influence of the shock are found. For these cases, the regions affected by the shock are removed and replaced with a third order polynomial.
6. The upper envelope of the modified TNTI from step 5 is found.

In step 6, enveloping is undertaken to ensure a one-to-one correspondence between the x location and the boundary layer height, and the upper envelop is chosen here since the contributions from the large δ-scaled turbulent features are warranted in the current analysis.

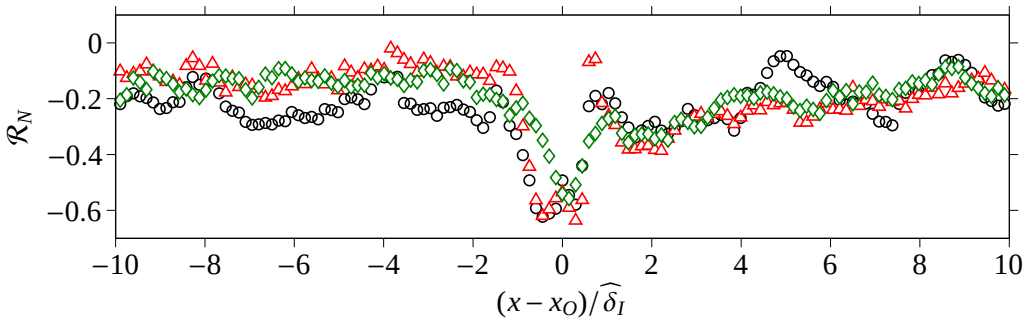

Figure 6: Two-point correlation coefficient between local boundary layer thickness and reflected shock location. Three choices for the measure of local boundary layer thickness are shown. ◊: upper TNTI envelope, △: z_{75}, i.e. z locations where $\widetilde{U} = 0.75U_\infty$ and ○: instantaneous displacement thickness.

Figure 5(b) shows the local kinetic energy for the $\widetilde{U}$ field shown in figure 4(a), while the location of the TNTI following step 4 is shown as the dotted (• • •) line. The dot-dashed line (- • -) show the upper envelope following step 6 (step 5 was not required for this particular instance). The inset shows an instance when the presence of the shock leads to an incorrect TNTI detection (solid line), and the adjusted TNTI location (dotted line) following step 5.

3.2 Influences of the incoming boundary layer

Figure 6 shows the correlation coefficient between the upper envelope of TNTI and the reflected shock location at various x locations (indicated as diamonds). The results suggest that the reflected shock location is well correlated ($|\mathcal{R}_N| > 0.4$) with the instantaneous boundary layer thickness immediately upstream of the shock. In addition, the instantaneous boundary layer thickness is influenced by the presence of the δ-scaled structures. Hence, the passage of low/high momentum large-scale turbulent features through the interaction region leads to the reflected shock to move upstream/downstream of the mean position, respectively. Note that, an alternate definitions for the boundary layer thicknesses such as the z locations where the velocity is 75 % of the incoming freestream velocity and the instantaneous displacement thickness, do not alter the $\mathcal{R}_N$ behaviour in the vicinity of the interaction region (see symbols △ and ○ in figure 6, respectively).

4 Wall-parallel PIV

In addition to the wall-normal PIV plane, wall-parallel measurements are undertaken at $z/\widehat{\delta_I} \approx 0.4$ and 1.7, as illustrated in figure 3. Both wall-parallel planes are intersected by the incident and reflected shock, and the planes are configured so that the plane closer to the wall resides within the boundary layer developing over the flat wall, while the plane away from the wall is at the freestream region. The combined FoV of 0.07 m × 0.16 m (corresponding to $4\widehat{\delta_I} \times 11\widehat{\delta_I}$) in the streamwise and wall-normal direction, respectively, with a scaling of 400 µm pixel^{-1} is obtained using two Imager sCMOS cameras. The laser, tracer particles and the PIV software used are the same as that for the wall-normal PIV. The initial and final window sizes are set to 64 × 64 pixels and 24 × 24 pixel, respectively, with an initial constant window shift to account for the mean velocity along the plane (Raffel et al., 2018). In addition, the time offset between double images is set at 2 µs resulting in a mean particle image shift of 26 and 30 pixels for the two wall-parallel planes, while all other settings are kept the same. Unlike the wall-normal plane PIV, a mirror-like surface is undesirable for the wall-parallel plane PIV, in terms of minimising the scattered light captured by the camera, and hence, the wall surface is painted matt black.

Figure 7 shows instantaneous examples of wall-parallel velocity fields in the outer region of the boundary layer at $z/\widehat{\delta_I} \approx 0.4$ (a) and in the freestream region at $z/\widehat{\delta_I} \approx 1.7$ (b). For (a) and (b), the instansteneous streamwise velocity field and its streamwise gradient are shown for the regions $y > 0$ and $y < 0$, respectively. The presence of the shock leads to a sharp change in $\widetilde{U}$, and in the freestream region the location of the shock can be identified based on $\partial\widetilde{U}/\partial x$ minima as illustrated in figure 7(b). However, as with the wall-normal plane, the change in $\widetilde{U}$ due to the shock within the boundary layer is more difficult to identify as its magnitude is within the order of the turbulent u fluctuations (see figure 7a), even though there is a clear

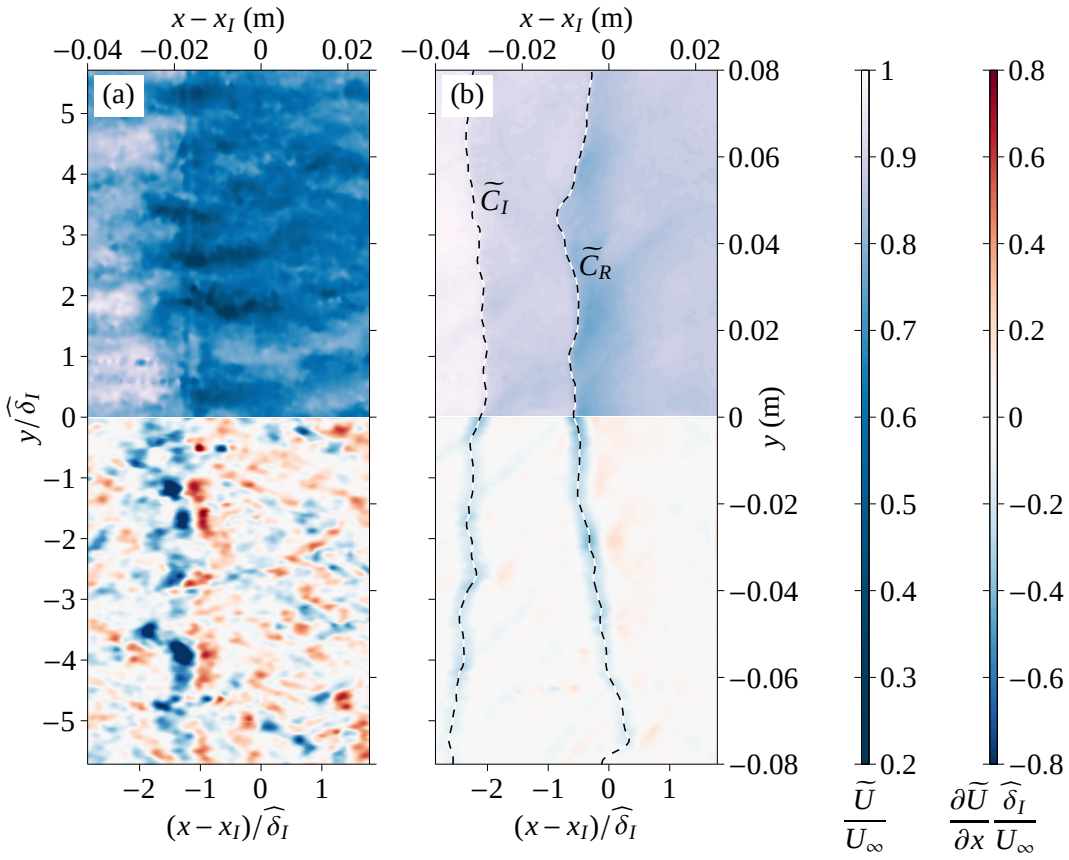

Figure 7: Instantaneous wall-parallel plane of the streamwise velocity and its streamwise gradient. The flow is from left to right and (a) and (b) correspond to z locations in the outer region of the boundary layer ($z/\widehat{\delta}_I \approx 0.4$) and the freestream region ($z/\widehat{\delta}_I \approx 1.7$), respectively. In (a) and (b), the streamwise velocity and its gradient are shown for the $y > 0$ and $y < 0$ regions, respectively.

influence from the shock on the mean field at this wall height. From figure 7(b), it is evident that the shock fronts undulate as a function of spanwise location, leading to a rippling pattern on a wall-parallel plane.

Figure 8(a) shows the pre-multiplied spanwise u-spectra, $k_y\phi_{uu}$, as a function of streamwise displacement relative to the shock locations. Here, k_y and λ_y correspond to the spanwise wavenumber and wavelength, respectively (i.e. $\lambda_y = 2\pi/k_y$). Upstream of the shock, in region ①, the u-spectra is close to x-invariant as the growth in the boundary layer with respect to x is minimal. Within the interaction region, region ②, strong u fluctuations that are energetic over a wide range of scales are introduced by the shocks. Downstream of the interaction region, the flow recovers towards a canonicals state and the excessive u fluctuations are dissipated and a near x-invariant u-spectra is observed at the most downstream location within FoV, indicated as region ③. Figure 8(b) shows the streamwise-averaged spectra over regions ①–③ as a function of λ_y. Notably, the dominant spanwise mode remains at $O(\widehat{\delta}_I)$ for regions ①–③, which coincides with the dominant spanwise length-scale of large and very-large scale motions present in wall-bounded flows (Kim and Adrian, 1999).

Figure 9(a) show the pre-multplied spanwise spectra of the incident (——) and reflected (- • -) shock locations. It should be noted that the incident and reflected shock locations, x_I^* and x_R^*, respectively, are based on wall-parallel PIV conducted at $z/\widehat{\delta}_I \approx 1.7$. Also shown overlaid is the u-spectra of the incoming boundary layer in the outer region of the boundary layer (• • •). From the figure, it is evident that the spanwise scales of the reflected shock location become increasingly energetic at wider spanwise length-scales when $\lambda_y/\widehat{\delta}_I \gtrsim 4$, while the energetic u motion of the incoming boundary layer remains approximately constant at these length-scales. Hence, the increase in the energetic content of x_R^* at these spanwise scales is unlikely to originate from the incoming boundary layer. In contrast to the u-spectra, an increased energetic contribution at a wider spanwise scale, similar to that observed for the reflected shock location, is also observed for the incident shock location. Thus, the data suggests that the increasing energetic contribution at a very-wide

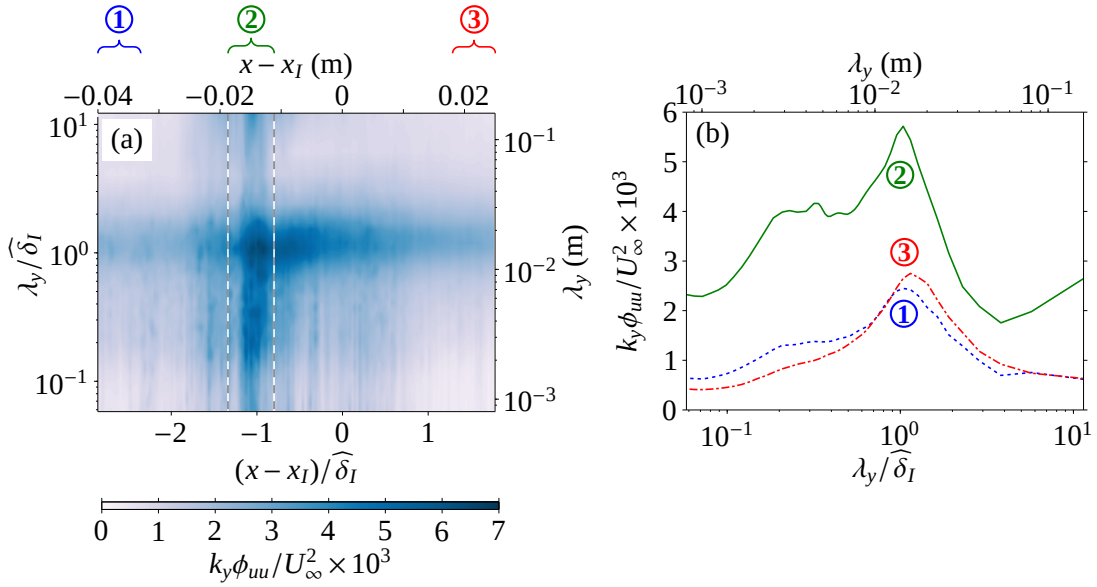

Figure 8: Pre-multiplied spanwise spectra of the streamwise velocity at $z/\widehat{\delta_I} \approx 0.4$. (a) Spanwise spectra as a function of x, where the vertical dashed lines denote the location of the incident and reflected shocks based on the mean U field. (b) Spatially-averaged one dimensional spectra over the streamwise domains ①, ② and ③ as indicated in (a).

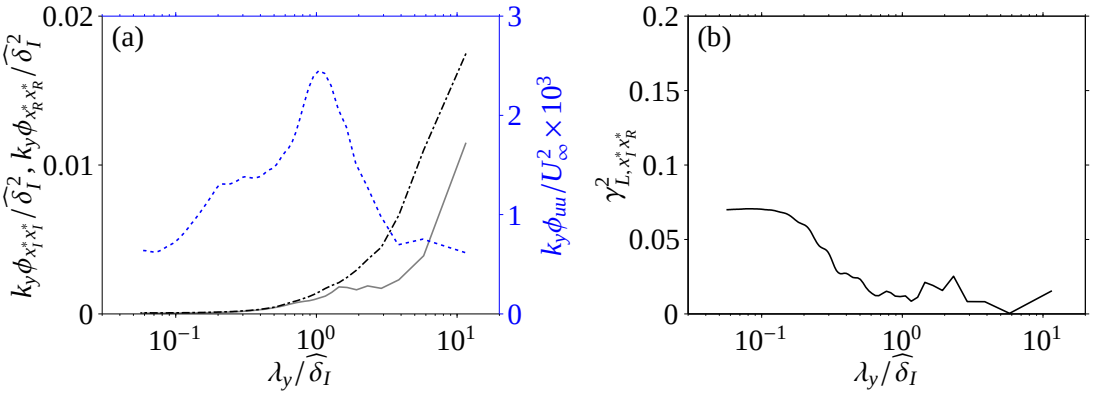

Figure 9: (a) Pre-multiplied spanwise spectra of the streamwise shock location captured on the plane $z/\widehat{\delta_I} \approx 1.7$. The solid (——) and dashed (- • -) lines correspond to the incident and reflected shock locations, x_I^* and x_R^*, respectively. Also shown in (a) as a dotted (• • •) line is the pre-multiplied u-spectra for the incoming boundary layer at $z/\widehat{\delta_I} \approx 0.4$ (i.e. u-spectra corresponding to region ① from figure 8b). (b) Linear coherence spectra of incident and reflected shock locations.

spanwise scale ($\lambda_y/\widehat{\delta_I} > 4$) for the reflected shock is due to influence of increasing energetic content for the incident shock at these scales. Figure 9(b) show the linear coherence spectra of the incident and reflected shock location. Here, the linear coherence spectra, $\gamma^2_{L,x_I^*x_R^*}$ is defined as

$$\gamma^2_{L,x_I^*x_R^*}(\lambda_y) = \frac{\left|\phi_{x_I^*x_R^*}(\lambda_y)\right|^2}{\phi_{x_I^*x_I^*}(\lambda_y)\,\phi_{x_R^*x_R^*}(\lambda_y)}, \tag{2}$$

where $\phi_{x_I^*x_R^*}$ corresponds to cross-spectrum of the incident and reflected shock locations while $\phi_{x_I^*x_I^*}$ and $\phi_{x_R^*x_R^*}$ denote the spectra of the incident and reflected shock locations, respectively, and the vertical bars ($|\,|$) designate modulus. By definition $0 \le \gamma^2_{L,x_I^*x_R^*} \le 1$, and here may be interpreted as a square of scale-specific

correlation coefficient (Bendat and Piersol, 2010; Baars et al., 2017). Hence, although the very-wide scales in x_R^* are influenced by x_I^*, the relation is not linear in nature.

5 Summary and conclusions

Experimental investigation of shock wave boundary layer interaction (SWBLI) for a reflection shock configuration at Mach 2 is presented. For the current configuration, an oblique incident shock impinges on a canonical compressible boundary layer, leading to a formation of a reflected shock upstream of the incident shock foot (see figure 3). A particle image velocimetry (PIV) technique is used to examine velocities on a plane that extends several boundary thicknesses upstream and downstream of the shock. Furthermore, to ensure a good spatial resolution to capture the small-scale turbulent features, a multi-camera approach is used where the field of view is constructed by combining the images from eight cameras.

One of the striking features of SWBLI is the oscillation of the shock front, which can lead to a large dynamic pressure loading and a modification to the heat transfer. In order to examine the mechanisms responsible for the shock oscillations, the current experiments are designed to simultaneously capture the shock location and the turbulent features residing within the boundary layer, as illustrated in figure 4. Our analysis shows that the instantaneous location of the reflected shock is dependent on the on the local boundary thickness of the incoming boundary layer (see figure 6). Since the instantaneous boundary layer thickness is influenced by the presence of the δ-scaled structures, a passage of low/high momentum very-large-scale turbulent feature through the SWBLI region leads to a change in the local boundary layer thickness, resulting in the reflected shock to move upstream/downstream of the mean location.

Wall-parallel PIV is used to investigate the spanwise characteristics of the shock and its interaction with the boundary layer and the large scale structures there in. While the shocks can be instantaneously identified in the freestream region, the streamwise velocity fluctuations (u) in the outer region of the boundary layer (at a wall height equal to 0.4 boundary layer thickness) are dominated by turbulent fluctuations, making detection of instantaneous u contribution from the shock difficult, even though there is a clear influence on the mean U field. In addition, the shocks introduce u fluctuations across a wide range of spanwise scales.

The spanwise spectra of the reflected shock, shown in figure 9, indicates a large energetic contribution beyond the dominant spanwise scales in the velocity fluctuations of the incoming boundary layer. For the present experiment, the incident shock itself oscillates, unlike in the past investigations, to mimic a common scenario in an engineering application. Thus, these scales are thought to be energised by influence from the oscillating incident shock where it also exhibits a large energetic contribution at these spanwise scales. However, the influence of the incident shock is found to be non-linear in nature due to the presence of turbulence.

Acknowledgements

This work is partly supported by the Priority Programme SPP 1881 Turbulent Superstructures funded by the German Research Foundation (Deutsche Forschungsgemeinschaft – DFG) under the project number KA1808/21-1.

References

Baars WJ, Hutchins N, and Marusic I (2017) Self-similarity of wall-attached turbulence in boundary layers. *J Fluid Mech* 823:R2

Bendat JS and Piersol AG (2010) *Random data: analysis and measurement procedures*. John Wiley & Sons. 4 edition

Bross M, Scharnowski S, and Kähler CJ (2019) Mach number influence on large-scale structures in ZPG turbulent boundary layers. in *Proc. 13th Int. Symp. Part. Image Velocimetry*

Dupont P, Haddad C, and Debieve JF (2006) Space and time organization in a shock-induced separated boundary layer. *J Fluid Mech* 559:255–277

Humble RA, Elsinga GE, Scarano F, and Van Oudheusden BW (2009) Three-dimensional instantaneous structure of a shock wave/turbulent boundary layer interaction. *J Fluid Mech* 622:33–62

Kähler CJ, Sammler B, and Kompenhans J (2002) Generation and control of particle size distributions for optical velocity measurement techniques in fluid mechanics. *Exp Fluids* 33:736–742

Kähler CJ, Scharnowski S, and Cierpka C (2012) On the uncertainty of digital PIV and PTV near walls. *Exp Fluids* 52:1641–1656

Kim KC and Adrian RJ (1999) Very large-scale motion in the outer layer. *Phys Fluids* 11:417–422

Muck K, Bogdonoff S, and Dussauge JP (1985) Structure of the wall pressure fluctuations in a shock-induced separated turbulent flow. in *23rd Aerosp. Sci. Mtg.*. page 179

Piponniau S, Dussauge JP, Debieve JF, and Dupont P (2009) A simple model for low-frequency unsteadiness in shock-induced separation. *J Fluid Mech* 629:87–108

Raffel M, Willert CE, Scarano F, Kähler CJ, Wereley ST, and Kompenhans J (2018) *Particle image velocimetry: a practical guide*. Springer

Reuther N and Kähler CJ (2018) Evaluation of large-scale turbulent/non-turbulent interface detection methods for wall-bounded flows. *Exp Fluids* 59:121

Scharnowski S, Bross M, and Kähler CJ (2019) Accurate turbulence level estimations using PIV/PTV. *Exp Fluids* 60:1

Thomas FO, Putnam CM, and Chu HC (1994) On the mechanism of unsteady shock oscillation in shock wave/turbulent boundary layer interactions. *Exp Fluids* 18:69–81